EXPERIMENTAL INVESTIGATION OF LOW SPEED MODEL PROPELLER SLIPSTREAM AERODYNAMIC CHARACTERISTICS INCLUDING FLOW FIELD SURVEYS AND NACELLE/WING STATIC PRESSURE MEASUREMENTS

Ingemar Samuelsson
FFA, The Aeronautical Research Institute of Sweden
Bromma, Sweden

Abstract

A low speed wind tunnel investigation of propeller slipstream aerodynamic characteristics has been carried out at FFA, Sweden. The wind tunnel tests were performed with different nacelle/wing combinations and a model propeller (model scale 1:5). The tests comprise slipstream flow field surveys (by means of a five-hole pressure probe) and static pressure measurements on slipstream washed nacelle and wing surfaces. Also the propeller thrust and torque were measured.

The results show that the distributions of the slipstream static and total pressures and velocities are considerably influenced by the mutual interaction between the slipstream flow and adjacent nacelle and wing surfaces.

The design of the near-propeller shape is shown to be very influential on the development of the slipstream-induced nacelle lateral loads (side force and yawing moment).

It is also shown that there is a considerable azimuthal variation of slipstream characteristics (pressures, velocities and swirl angles) due to the non-axisymmmtrical nacelle shapes, especially near to the propeller disk.

It is believed that the obtained results perhaps could be of some value in the understanding of the rather complex propeller slipstream flow physics and also to provide some guidance for the design of propeller nacelle shapes.

Nomenclature

A	aspect ratio of wing = b^2/S	[-]
A	area	[m^2]
b	wing span (= 2m)	[m]
c	wing chord (= 0.5 m)	[m]
C_F	thrust coefficient = $T/(q_\infty S)$	[-]
C_p	pressure coefficient = $(p-p_\infty)/q_\infty$	[-]
C_P	power coefficient = $P/(\rho_\infty n^3 D^5)$	[-]
C_T	thrust coefficient = $T/(\rho_\infty n^2 D^4)$	[-]
D	propeller diameter (=0.640 m)	[m]
J	advance ratio = $U_\infty/(nD)$	[-]
n	propeller rotational speed (revs/s)	[1/s]
N	propeller RPM	[1/min]
p	static pressure	[Pa]
p_t	total pressure	[Pa]
P	propeller shaft power = ωQ	[W]
q_∞	free stream dynamic pressure = $=0.5\ \rho_\infty U_\infty^2$	[Pa]
q_0	free stream dynamic pressure = q_∞	[Pa]
Q	propeller shaft torque	[Nm]
r	radius	[m]
R_p	propeller radius (= 0.320 m)	[m]
S	reference area (= 1.672 m^2)	[m^2]
T	propeller thrust	[N]
u_r	radial velocity	[m/s]
u_t	tangential (azimuthal) velocity	[m/s]
u_x	axial velocity	[m/s]
U	flow velocity	[m/s]
x,y,z	nacelle fixed coordinate system, (see Figure 5)	[m]
α	angle of attack	[°]
β	side slip angle	[°]
$\beta_{.75}$	propeller blade pitch at 75 % propeller radius	[°]
ε	swirl angle = $-\tan^{-1}(u_t/u_x)$	[°]
η	propeller efficiency = TU_∞/P	[-]
κ	normalized propeller torque loading	[-]
ρ	fluid density	[kg/m^3]
τ	normalized propeller thrust loading	[-]
φ	angular position	[°]
ω	propeller shaft angular speed	[rad/s]

Subscripts

∞	free stream conditions
s	pertaining to probe position
r	radial
t	tangential (azimuthal)
x	axial
tot	total

Symbols

Δ	difference

Abbreviations

RPM	revolutions per minute
ID	inner diameter
OD	outer diameter
TE	trailing edge

I. Introduction

The recent development of propeller-driven aircraft, especially for the commuter market, has created an interest in and concern about the aerodynamic effects due to the propeller slipstream. These effects are concentrated to the prop-washed areas on the nacelles, wings and stabilizers. For instance, due to high loading of the propellers and therefore also highly energe-

tic propeller slipstreams there could be rather large asymmetrical loads on the motor nacelle, especially so for asymmetrical nacelle shapes.

In order to gain some physical insight to this and related phenomena associated with the propeller slipstream, several low speed wind tunnel tests have been conducted at FFA during recent years. These studies have been carried out with different schematic nacelle/wing combinations. The investigations comprised measurements of both wing and nacelle surface static pressures and propeller slipstream flow field surveys. The slipstream flow fields were surveyed by means of a five-hole pressure probe, resulting in distributions of slipstream velocities and pressures.

Besides helping in the understanding of the fluid mechanics of the propeller slipstream flow, the slipstream surveys also serve as test cases for numerical methods for prediction of propeller slipstream aerodynamic interference effects. Such methods are currently being developed in this country.

II. Experimental Technique and Setup

Wind Tunnel

The tests were carried out in the FFA low speed wind tunnel LT1. The test section of this wind tunnel has a circular cross section with a diameter of 3.6 m. The maximum speed is about 85 m/s.

Wind Tunnel Model Installation

The models were installed in the wind tunnel by means of a tail sting arrangement (Fig. 1). The sting was mounted on a movable sting frame. The attitude (α and β) of this sting frame is controlled by means of servo motors via a strut and suspension wires.

Model Propeller Drive Unit

The propeller was driven by a hydraulic motor housed inside the model nacelle. The compressed hydraulic oil was fed to the motor by a pump situated outside the tunnel via hoses and tubes inside the sting. The hydraulic pump is power rated to about 75 kW, but the maximum propeller shaft power in this test was about 45 kW.

Model Nacelle/Wing

In total four different nacelle/wing combinations were tested (for geometry, see Figure 2), both prop-on and prop-off.

The baseline nacelle was an axisymmetrical body, designed as a "minimum body" to house the hydraulic motor and with room for the sting mounting, the Scanivalves and associated plastic tubing for the pressure taps on the nacelle surface, etc. Inside the nacelle there were also provisions made for the proper alignment of the nacelle with the propeller axis and the sting.

For the "high" nacelle the two nacelle halves for the baseline nacelle were separated by a cylindrical middle part. In this case the lower nacelle part was cut in the near-propeller region and here the middle part was provided with a "chin", thus forming a smoothly rounded transition region between the nacelle parts. No air inlet was simulated.

For both nacelle layouts two unswept wing halves could be mounted. The wing had a rectangular planform with chord = 0.5 m and span = 2.0 m., thus giving an aspect ratio of 4. The airfoil section was NACA $63_{(10)}$A-012.

Model propeller

The four-bladed propeller is a 20% scale model of the original propeller for the SAAB 340 commuter aircraft (full scale diameter = 126" = = 3.20 m). This 0.64 m diameter model propeller has been used before in the wind tunnel development work of the SAAB 340. The aluminium model propeller (and the full scale propeller made of composite materials) was designed and manufactured by the British firm Dowty Rotol, Ltd. The propeller is thought to be a typical example of the highly-loaded propellers for the new generation of medium-speed commuter aircraft.

Model Instrumentation

The propeller thrust and shaft torque were measured by means of strain-gauge elements mounted on the propeller shaft inside the spinner. Since these balance elements were rotating with the propeller, the balance signals were transmitted through a slip ring unit. The propeller RPM was measured by means of a magnetic pickup mounted on the hydraulic motor.

The nacelle and wing surface pressures were measured by means of the Scanivalve technique. The Scanivalves were mounted inside both the nacelles and the wing.

Five-hole pressure probe

The propeller slipstream flow field was surveyed by means of a traversing five-hole pressure probe. The probe layout is depicted in Fig. 3. Five nickel tubes (OD = 1 mm, ID= 0.7 mm) were soldered together in a cross configuration. The tubes surrounding the central tube were beveled 45° and the central tube was cut perpendicularly to the tube centre line. The spaces between the assembled tubes were filled with epoxy resin and hand formed to give a smooth contour.

Five-hole probe calibration

The five-hole probe was calibrated in the low speed wind tunnel by putting it at different angles to the free stream velocity vector. The calibration was carried out at several free stream speeds and with the flow angles covering the range of -40° to +40° (see Figures 3 and 4 for definition of angles and examples of calibration data). The probe positioning and the pressure signal acquisition were controlled by the wind tunnel computer. In order to reduce the effect of experimental scatter several data points were acquired at each of the calibration points and mean values were subsequently formed.

The calibration procedure is described in detail in [2].

Probe traversing mechanism

The probe was mounted on a cranked sting and plastic hoses connected the probe holes at the probe tip to pressures transducers. The probe sting was attached to a special traversing mechanism. This mechanism is attached to the model sting by means of clamps. The probe sting was traversed along the radial direction by means of a ball screw mechanism driven by a DC motor attached to one of the clamps. The radial displacement of the probe sting was sensed by a linear potentiometer glued onto the rear side of the downstream radial steel rod of the ball screw mechanism.

The axial and azimuthal positions of the traversing mechanism was changed by sliding and rotating it on the model sting. The axial position of the probe could also be changed by sliding the probe sting on the traversing mechanism. For a more detailed description of the probe traversing mechanism, see Ref [2].

Data acquisition and reduction

During the wind tunnel runs either the signals from Scanivalve pressure transducers or the probe pressures were multiplexed, A/D converted and then stored in the computer memory. In a few cases the intrusive effects of the probe mounting was checked and both Scanivalve pressures and the probe pressures were recorded simultaneously. Since these intrusive effects were rather small, the measurements of nacelle/wing surface pressures and the slipstream flow field surveys were conducted separately.

For both types of measurements, however, the wind tunnel speed and the propeller RPM were of course recorded.

For the slipstream flow field survey, about 350 points along the chosen radial survey line were scanned in each run, beginning near the nacelle surface and ending at about 1.6 times the propeller radius (that is, outside the propeller slipstream).

The obtained five-hole pressures were then converted to total slipstream speed and flow angles, slipstream total, static and dynamic pressures by means of prestored probe calibration data.

III. Scope of test

The layouts for the tested configurations are shown in Fig. 2. The complete test programme for nacelle/wing surface pressure measurements and the propeller slipstream flow field surveys are given in Refs [1] and [2]. Out of this rather large amount of acquired data, results for the following test point are selected for the present paper:

$\alpha = \beta = 0^o$
$\beta_{.75} = 29^o$ (prop blade pitch)
$U_\infty = 50$ m/s
$N = 6650$ RPM

With the selected propeller this gives the following propeller characteristic values:

$C_T = 0.23$ (thrust coefficient)
$J = 0.70$ (advance ratio)
$C_P = 0.25$ (power coefficient)

At this chosen test point, the propeller slipstream flow fields were surveyed for the four configurations in (at least) three different downstream planes perpendicular to the propeller axis.

The selected test point is concerned with a rather high power flow condition (C_T=0.23, C_P=0.25, J=0.70). This is thought to be approximately corresponding to the power setting during climb-out but at $\alpha=0^o$ and with wing trailing flap angle $=0^o$. This particular case was chosen so that the propeller slipstream would be rather energetic (that is, with large velocities within the slipstream) in order to make the slipstream effects on the nacelle and on the wing clearly distinct. It was also recognized that the highly loaded slipstream could represent a challenging (not to trivial) flow test case for the numerical prediction methods currently being developed.

For definition of coordinate systems and flow velocity components, see Figure 5.

IV. Results and discussion

General characteristics of the propeller slipstream flow field

As an example of the general characteristics of the propeller slipstream flow field, some results for CONF1 (axisymmetrical nacelle, no wing) are presented, Figures 6a, b,c. In this case the survey plane is rather close to the propeller disk plane (downstream distance = 14 % prop radius).

Slipstream pressures

As can be seen in Fig 6a, and which of course is expected, there is an increased total pressure within the slipstream, with a maximum in this case of about 1.9 q_∞ at about 70 % prop radius. The pressures (total, static and dynamic pressures) all decrease markedly towards the slipstream boundary. In this region both the total and static pressures also exhibit sharp minima. These minima, however, do not occur at the same radius. The total pressure minimum seems to occur at a slightly larger radius than the static pressure minimum. Outside the minimum the total pressure rather quickly goes to zero. Of course, this is partly an effect of the data reduction procedure for the total pressure, as the total pressure data have been reduced with the mean of the total pressure at the 20 last points in the radial traverse. This is thought to be justified by the conceived non-existence of physical mechanism outside the slipstream that could generate any total pressure changes. Also, the behaviour of the total pressure outside the slipstream boundary, with a near constant value = zero, seems to make this particular data reduction procedure plausible.

Slipstream velocities

In Fig. 6b the slipstream velocity vectors are depicted in two projections, one showing the superimposed axial and radial components and the other the superimposed tangential and radial velocity components (that is, the cross-flow velocities). As can be seen in this figure there is a large increase of the axial velocity in the slipstream (in this case about 47 % increase over the free stream speed at about 3/4 prop radius). This obviously indicates the high power flow condition. Towards the slipstream boundary the axial velocity component exhibits a very sharp radial gradient. Outside the slipstream boundary the axial velocity first displays a minimum and then seems to asymptotically assume the free stream speed at greater radii.

The cross-flow plot clearly shows the co-rotational character of the slipstream, that is, the slipstream rotates in the same sense as the propeller. The maximum tangential speed is nearly 40 % of the free stream speed at the innermost radii of the slipstream. Outside the slipstream boundary the tangential velocity component is effectively equal to zero.

Close to the nacelle the slipstream flow direction is governed by the shape of the nacelle but towards and outside the slipstream boundary there is an inward flow, thus confirming the "sink" effect of the propeller flow.

The radial velocity component exhibits a rather interesting feature in the close proximity of the slipstream boundary, see Fig 6c. At the boundary passage the radial velocity component displays three sharp gradients. This is interpreted as an effect of passing through the viscous cores of the propeller tip vortices.

As can be seen in Fig. 6c the swirl angle, $\varepsilon = -\tan^{-1}(u_t/u_x)$, seems to decrease monotonically from the maximum value (19°) at the innermost radii to zero outside the slipstream.

As is also evident in this figure, the slipstream (at this axial survey station) has contracted to about 96 % of the prop radius (that is, to about 92 % of the disk area).

The above description of the general characteristics of the propeller slipstream flow is rather representative for many of the surveyed slipstream flow fields. However, as will be shown, there are some important influences on the detailed slipstream flow structures from e.g. nacelles and presence and location of the wing in the slipstream.

Check of the measured slipstream total pressures and velocities

In order to check whether the obtained slipstream total pressure levels are reasonable, a few of the measured total pressure distributions were integrated over the slipstream area to see if the propeller thrust could be recovered this way. By assuming that the thrust T produced by the propeller is manifested as a total pressure increase in the slipstream and that the differential thrust dT over an annular slipstream area, $dA = 2\pi\, r\, dr$, is equal to

$$dT = \Delta p_{tot} \cdot dA = \Delta p_{tot} \cdot 2\pi r dr, \qquad (1)$$

one obtains for the total thrust T:

$$T = \int \Delta p_{tot} 2\pi r dr,$$

where

$\Delta p_{tot} = p_{tot}(r) - p_{tot,\infty}$

$p_{tot}(r)$ = slipstream total pressure at radius r

$p_{tot,\infty}$ = free stream total pressure.

The integration should be extended from the nacelle surface to $r=\infty$. In this case the integral was evaluated along the experimentally given radial survey line, that is, from about $r/R_p \approx 0.28$ to $r/R_p \approx 1.60$. The value of the integral is not sensitive to the upper limit since the total pressure increase Δp_{tot} quickly assumes zero value outside the slipstream boundary.

The total pressure data given in Figure 6a were integrated in this way and the obtained integrated thrust was about 4 % higher than the balance thrust:

C_T(integrated) = 0.241

C_T(measured) = 0.232

This is considered as a rather good agreement (the difference is believed to within the experimental scatter).

Also the propeller torque was checked by means of integration of the slipstream velocities. If one assumes the slipstream flow is axisymmetrical (axisymmetrical nacelle geometry and axisymmetrical onset flow), the following expression for the propeller torque is obtained from consideration of the conservation of angular momentum in the flow:

$$dQ = \rho \cdot u_x \cdot u_t \cdot r dA = \rho \cdot u_x \cdot u_t \cdot 2\pi \cdot r^2 dr \qquad (2)$$

$$Q = \int \rho \cdot u_x \cdot u_t \cdot 2\pi \cdot r^2 dr$$

For the velocity data shown in Figure 6b the following results were obtained for the power coefficient C_P:

C_P(integrated) = 0.242

C_P(measured) = 0.248

The integrated value in this case agrees even better with the measured value than for the thrust (2 % lower value for the integrated value). Hence, it is believed that the slipstream pressures and velocities as obtained by the 5-hole probe could be used with some confidence. At least this conclusion is thought to be valid in some global (integral) sense. There is some concern about the spatial resolution cabability of the probe in the high-gradient flow areas, eg. towards the slipstream boundary, where there are considerable spatial variations of the flow quantities over the probe size. No special investigation concerning this has been carried out.

There is also some concern about the ability of the probe and the associated measuring system to capture the true time-averaged values of the inherently unsteady propeller slipstream flow quantities. Also, this matter has not been investigated, but it is believed that, in spite of the abovementioned uncertainties, the obtained data are realistic.

Propeller thrust and torque loadings (as obtained from slipstream surveys)

By using the equations (1) and (2) one obtains the following expressions for the thrust and torque loadings, respectively:

$$dT/dr = 2\pi r \Delta p_{tot}$$

$$dQ/dr = 2\pi r^2 u_x u_t.$$

These loadings are normalized to give:

$$\tau = d(T/T_{tot})/d(r/R_p) = R_p/T_{tot} \cdot dT/dr$$

$$\kappa = d(Q/Q_{tot})/d(r/R_p) = R_p/Q_{tot} \cdot dQ/dr$$

where T_{tot} and Q_{tot} are the total thrust respective total torque as obtained by integration over the slipstream. This normalization means that the integrals of τ and κ over the slipstream assume the value one:

$$\int \tau d(r/R_p) = 1$$

$$\int \kappa d(r/R_p) = 1$$

These non-dimensionalized loadings are shown in Figure 7 (the input data are taken from Figure 6). No scaling of the radius has been carried out in order to compensate for the contraction of the slipstream. As can be seen in Figure 7 the thrust and torque loadings are rather similar for $r/Rp<0.9$. Towards the high-gradient regions near the slipstream boundary the loadings differ. The thrust loading assumes negative values in the boundary region ('tip loss'). The negative thrust loading here integrates to about 0.4 % of the total integrated thrust. Outside the slipstream boundary the torque does not seem to vanish as it should. This is believed to be due to some experimental errors. E.g. there could be some upwash in the wind tunnel flow not accounted for in the definition of the wind tunnel angle of attack, meaning that the 5-hole probe will record a swirl angle $\neq 0$ outside the slipstream boundary. This negative torque loading outside the boundary integrates to about 2 % of the total torque.

IV.1 Results for CONF1

Axial development of slipstream characteristics

In Figure 8 the total and static pressures and the swirl angle are depicted vs radius for four different axial survey locations. As can be seen the maximum total pressures seem to be about the same for the four stations. There is, however, certain redistributions of the total pressure within the slipstream as it develops along the nacelle. One can also note that the gradients in the total pressure in the proximity of the slipstream boundary seem to become less sharp at the most downstream located survey stations. This is interpreted as an effect of the growth of the vortex cores due to viscous effects (diffusion). Due to these viscous effects there could also be a loss of total pressure in the streamwise direction.

The static pressure distributions show that there is a tendency for the static pressure to level out as the slipstream develops along the nacelle. Due to the thrust-producing mechanism of the propeller there is a overpressure ($C_p > 0$) in the slipstream flow close to the propeller disk. Due to the increasing nacelle diameter and slipstream contraction the slipstream flow accelerates up to the station of maximum nacelle diameter, that is, the static pressure decreases. Towards the end of the nacelle, with decreasing nacelle diameter, the flow is retarding and the static pressure increases again. However, the difference between the maximum and minimum static pressure along the radial survey line diminishes as the flow develops along the nacelle. As can be judged from the shapes of the C_p depressions in the tip vortex region, the vortex core radius seems to be increasing in the streamwise direction and at the same time the C_p depression seems to diminish.

Towards the downstream end of the nacelle the slipstream has contracted to about 92 % of the prop radius, that is, to about 84 % of the prop disk area. Due to the slipstream contraction and the nacelle shape the maximum velocities first increase along the nacelle and then decrease towards the end of the nacelle. It is believed that the slipstream contraction has not yet been completed at the most downstream survey location, mainly due to the fact the static pressure has not yet leveled off to $C_p=0$.

The swirl angle distributions versus slipstream radius are depicted in the lower part of Figure 8. As can be seen the maximum swirl angles are encountered close to the propeller disk plane. For the other survey locations further downstream there is an interesting feature in swirl distributions. Close to the nacelle surface the swirl angles for these three display a marked decrease. This is believed to be a combined effect of the presence of the propeller hub vortices as they revolve around the nacelle and the nacelle boundary layer.

IV.2 Results for CONF2

In Figure 9 results for eight probe traverses of the slipstream at different azimuthal positions for an axial survey station close to the propeller disk have been plotted. The onset flow is nominally axisymmetrical ($\alpha=\beta=0°$) but since this configuration (axisymmetrical nacelle with a mid-wing) is not strictly axisymmetrical, one could expect some non-axisymmetrical distributions of the slipstream quantities. However, since the wing is symmetrical, the resulting flow should possess anti-symmetry.

As can be seen for the total and static pressures and the swirl angle, the azimuthal variation of these quantities seems to be small at this survey

station close to the disk plane (and rather remote from the wing, 78 % wing chord upstream of the wing leading edge).

The observed small deviations are mainly attributed to experimental inaccuracy and errors associated with the experimental procedure. Each of the shown traverses were carried out as separate experiments. For each of the traverses the probe was mounted in the proper position (wind off/ stopped propeller) and then the wind tunnel and propeller speeds were adjusted to correct values. Then the probe was traversed along the radial direction. It is believed that errors incurred by this procedure (linear/angular probe position errors, wind tunnel/prop speed errors, varying ambient flow conditions, etc) do account for the major part of the observable deviations in the results. It is therefore difficult to infer any influences from eg the wing on the inflow at the propeller disk.

This is not to say, however, that the presence of the wing does not influence the axial development of the slipstream, as is evident in the next two Figures 10a and 10b. These Figures comprise the survey results in the wing quarter chord plane. The results for the upper half plane of the wing are shown in Figure 10a and for the lower half plane in Figure 10b.

As can be seen, there is a considerable azimuthal variation of the quantities shown. In this case there are some indications of anti-symmetrical flow conditions.

In Figure 11 the corresponding results for a survey plane located close to the wing trailing edge (5 % wing chord downstream of the TE) are shown. Also in this case there are some indications of anti-symmetrical flow. Here one can note that two of the radial traverses (for φ = 0° and 180°) are located in the extension of the wing plane and there are signs that this is in the wakes of the respective wing halves downstream of the TE. The total pressure distributions for these two wake runs are significantly dissimilar to the other runs at this station. Also the static pressure and swirl angle distributions for these two wing wake traverses deviate markedly (in shape and level) from the other runs.

Cross-flow velocity vectors

Figure 12 displays the cross-flow velocity vectors in the three survey planes in the slipstream. The slipstream flow seems to be 'sheared' by the wing, that is, the slipstream boundary is located at different spanwise stations on the upper and lower sides of the wing (on both the wing halves). One can also note the strong influence of the wing on the flow near the wing. Here the rotating slipstream flow is reversed. Close to the nacelle the co-rotating flow (even away from the wing) also seems to change direction. This could perhaps indicate the presence of the propeller hub vortices. For the survey plane downstream of the wing TE (the lower part of Figure 12) one can also note the sheared slipstream boundary. It is evident that there is still a considerable amount of swirl left in the slipstream, implying, in this particular case, that the swirl recovery due to the wing is far from complete.

Effect of angle of attack on total pressure distributions

As an example of the effect of angle of attack on the total pressure distributions Figure 13 is shown. This Figure displays the total pressures as isobar maps over the slipstream for α = 0° and 10° for CONF2 at the survey plane closest to the propeller disk plane (downstream distance = 14 % prop radius). When the propeller axis is inclined to the onset flow, there will be different flow conditions for the up- and down-going blades of the propeller. For a right-going propeller (as the present one) put at positive angle of attack the resulting flow angles and velocities will be higher for a down-going blade than for a up-going blade. This will result in a higher loading for the down-going blade than for the up-going one, leading to a higher level of total pressure for the down-going blade. Hence, in this case, the total pressures in the right-hand half of the slipstream should be higher than in the left-hand half. At the disk plane, where these total pressures are generated, the total pressure should be approximately symmetrically distributed around the horizontal line (neglecting interaction effects from the nacelle and the wing).

Since the slipstream field rotates (in the same sense as the propeller) the total pressure field will be displaced in the slipstream rotational direction. This is clearly shown in Figure 13. The upper part of this Figure 12 shows the total pressure for α = 0°, where the isobars are approximately circular in shape. For α = 10° (lower part of Figure 13) there is distinct increase of total pressure in the right-hand half of the slipstream and the total pressure field is displaced. It is believed that, since the measured total thrusts (from the thrust balance) for these both angles of attack are about the same, integrations of the total pressure distributions over the slipstream will yield about the same thrust also. However, this has been not carried out for these two cases.

IV.3 Results for CONF3

Axial development of the slipstream cross-flow

Figure 14 shows the cross-flow velocity vectors in three different axial survey planes: close to the prop disk plane (upper part of the Figure), about mid-nacelle (middle part) and close to the downstream end of the nacelle (lower part). Also the nacelle surface static pressures are shown for the respective survey stations (values taken from Reference [1]).

As can be seen the rotational symmetry of the slipstream flow is to a large extent influenced by the nacelle shape. By comparing results for the axisymmetrical nacelle (wing off:CONF1) (Fig. 6b) and the 'high' nacelle (wing off: CONF3) (Fig. 14) at the survey plane close to the disk plane, one can note large differences. The results for the axisymmetrical nacelle (CONF1) are for just one radial survey line, but as both the nacelle and the onset flow in this case both are axisymmetrical, the shown cross-flow is representative for the whole survey plane. For the non-axisymmetrical nacelle there is a large

azimuthal variation of the cross-flow. Also, this variation seems to be more pronounced in the lower half of the slipstream than in the upper half. This does of course reflect the fact that the nacelle geometry is more complex in the lower part, with its rapidly varying cross-section, than in the upper part.

Also for the nacelle surface pressures there is large asymmetry. On the right-hand half of the nacelle cross-section the pressure are much larger than on the left-hand half, resulting in a side force on the nacelle. Since the asymmetrical nacelle acts like a 'guiding vane' and the rotating slipstream flow set up a flow angle from right to left, there is flow around the 'chin' of the lower part of the nacelle and this will give the above mentioned side force. The magnitude of this side force is also thought to be affected by the varying total pressure in the slipstream, in addition to the swirl angle.

Both the total pressure and swirl angles within the slipstream are believed to be established by the interaction between the propeller onset flow and by flow perturbations induced by the nacelle geometry.

Further downstream of the nacelle there is still an asymmetrical flow around the nacelle with distinct 'shear' of the slipstream boundary. The nacelle surface static pressure magnitudes decrease towards the downstream locations and also tend to be equalized around the nacelle perimeter.

IV.4 Results for CONF4

Axial development of the propeller slipstream cross-flow

Figure 15 shows the cross-flows for CONF4, depicted at the same three axial surveys plane locations as for CONF3. By comparing the cross-flows for CONF3 (no wing) and for CONF4 (low-wing) at the near-disk location (at 14 % prop radius downstream distance) the differences between these cases are small. It seems that the flow in this region near to the propeller to a great extent is governed by the nacelle geometry in this area and not so much by the more remote downstream located wing. This is so despite the fact that there is a flow around the wing leading edge and hence also a circulation around the wing. Evidently this bound circulation does not to any appreciable degree influence the flow near to the propeller (at least not so for this case with $\alpha = 0^{o}$).

For the mid-nacelle position there is, of course, a large wing influence on the cross-flow since the flow cannot penetrate the wing. As for CONF2 there is significant amount of 'shear' of the slipstream boundary. One can also note for CONF4 that the cross-flow velocity vectors are reversed near to the nacelle surface at the upper half of the nacelle. Again this interpreted as an effect of the propeller hub vortices.

For the aft wing survey location (5 % wing chord downstream distance of the wing TE) there is a distinct displacement of the slipstream boundary to the right (looking upstream). As for CONF2 (symmetrical nacelle with mid-wing) there still seems to be a significant amount of swirl in the slipstream downstream of the wing. The degree of swirl recovery also seems to be higher at the left-hand side of slipstream since the magnitudes of the tangential velocity vectors are lower here. This is thought to be an effect of the low-wing arrangement for CONF4 since for this case the flow boundary conditions are different on the left-hand and the right-hand half of the slipstream. This is also thought to be confirmed by the wing pressure distributions (not shown, see Ref [1]). These pressure distributions show that the magnitudes of the positive lift on the left wing half are higher than the magnitudes of the negative lift on the right wing half. If the wing halves were placed symmetrically in the propeller slipstream, these magnitudes would have been equal. Consequently, the flows around the respective wing leading edges would not be same (apart from flow direction), that is, the magnitudes of the slipstream induced wing leading edge flow angles are different on the two wing halves. Hence, the chordwise wing leading edge suction forces would also be different (but both are directed upstream), which is to say that the amount of swirl recovery is different on the two sides.

V. Concluding remarks

Low speed wind tunnel investigations of propeller slipstream flows around different nacelle/wing combinations have been carried out. Some of the main conclusions that can be drawn from these tests are:

* The distributions of velocities and pressures within the propeller slipstream are to a large extent influenced by the nacelle shapes. If the nacelle geometry is rapidly varying in the close proximity of the disk plane (as it often is), there could be a large effect in the inflow to the propeller. This propably leads to a large variation of the propeller blade forces and moments, thereby leading to shaft vibratory motions and effecting the fatigue life of propeller. The azimuthally varying blade loadings could perhaps also generate additional airborne noise.

* An asymmetrical and rapidly varying nacelle geometry close to the disk plane also means that there will be rather large asymmetrical loads on the nacelle. The cause of these loads is thought to be a 'guiding vane' effect of the asymmetrical nacelle as a reaction to the rotating slipstream flow.

* The influence of the wing being washed by the propeller slipstream on the inflow to the propeller seems to be small, at least for small angles of attack and with the wing located at 'normal' downstream distances from the propeller (in this test the wing leading edge was at 87 % wing chord distance from the disk plane = 136 % prop radius).

* Within the slipstream there are rather large spatial gradients in velocities and pressures, especially so towards the slipstream boundary. However, these gradients are thought to be dependent on the loading

of the propeller since the encountered maximum velocities are closely related to this loading.

* The downstream located wing has a strong influence on the location of the propeller slipstream boundary in the vicinity of the wing. The boundary seems to be 'sheared' at the passage of the wing, so that the slipstream boundaries at the upper and lower wing surfaces are at different spanwise stations.

* Due to the rotating slipstream there is also a certain amount of swirl recovery attributed to the induced flow around the wing leading edges. The investigation shows that, for the tested case with J≈0.70, there still remains a considerable amount of swirl in the slipstream downstream of the wing.

References

[1] Samuelsson, I. "Low Speed Wind Tunnel Investigation of Propeller Slipstream Aerodynamic Effects on Different Nacelle/Wing Combinations".

Part 1: "Total Forces and Moments and Pressure Distributions on Nacelle/Wing at Different Angles of Attack and at Different Thrust Coefficients".

FFA TN 1987-22, Bromma, Sweden, 1987.

[2] Samuelsson, I. "Low Speed Wind Tunnel Investigation of Propeller Slipstream Aerodynamic effects on Different Nacelle/Wing Combinations".

Part 2: "Propeller Slipstream Flow Field Surveys (Velocity Components, Dynamic, Total and Static Pressure Distributions)".

(to be published)

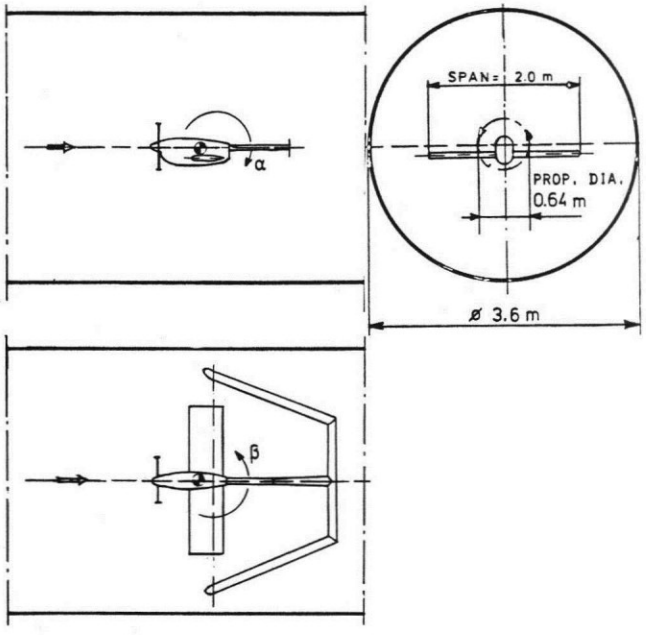

Figure 1 Model installation in the wind tunnel (cont.)

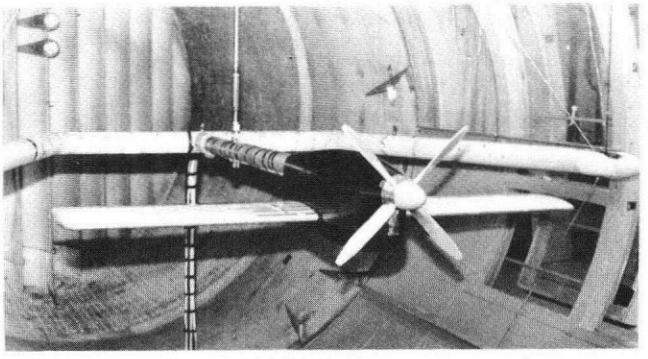

Figure 1 Concl.

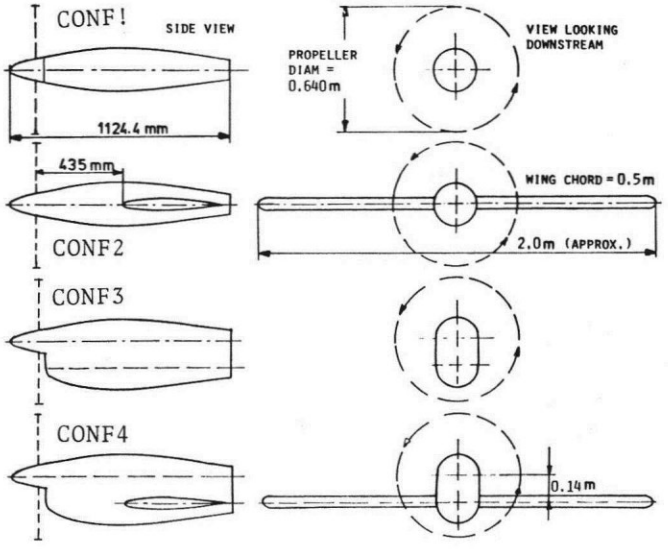

Figure 2 Tested model nacelle/wing combinations

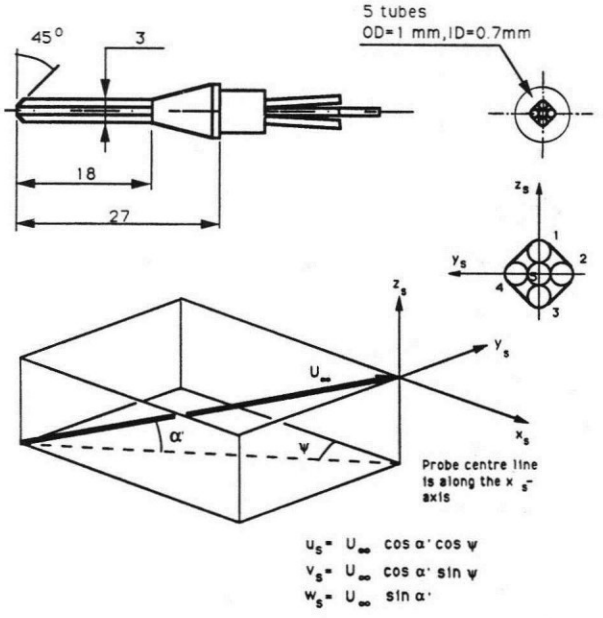

Figure 3 Five-hole probe layout and definition of probe coordinate system (including flow angles)

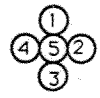

Five-holed probe
(facing downstream)

Measure p_1 through p_5
Determine minimum and average pressures:

$p_{min} = \min(p_1,p_2,p_3,p_4)$
$p_{aver} = 1/4 \cdot (p_1+p_2+p_3+p_4)$

$F_A = (p_3-p_1)/(p_5-p_{min})$ $\quad F_P = (p_2-p_4)/(p_5-p_{min})$

$F_Q = (p_5-p_{aver})/q_\infty$ $\quad F_H = (H_\infty-p_5)/(p_5-p_{min})$

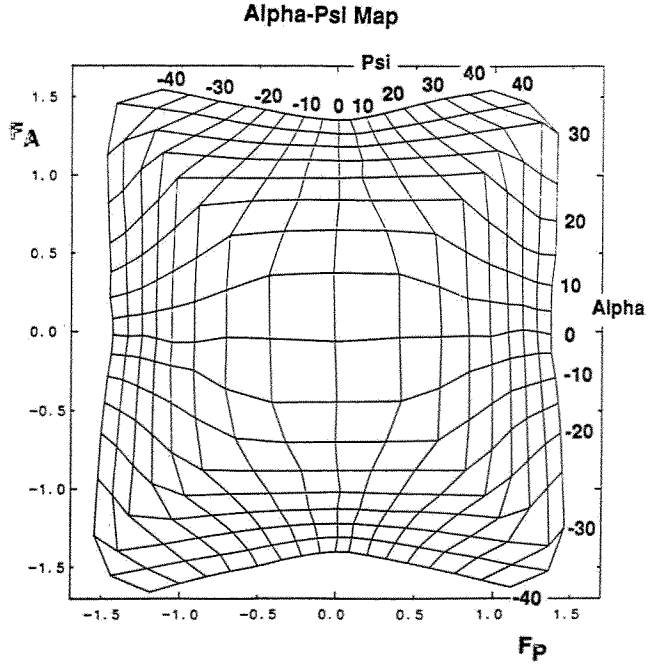

Figure 4 Five-hole calibration procedure and example of probe calbration data

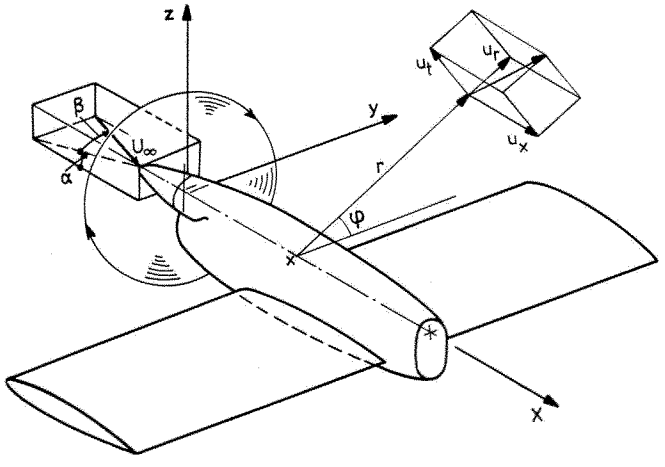

Figure 5 Definition of model coordinate system and flow velocity components (in cylindrical coordinates (x,r,φ)). The origin of the coordinate system is located 35 mm downstream of the prop disk

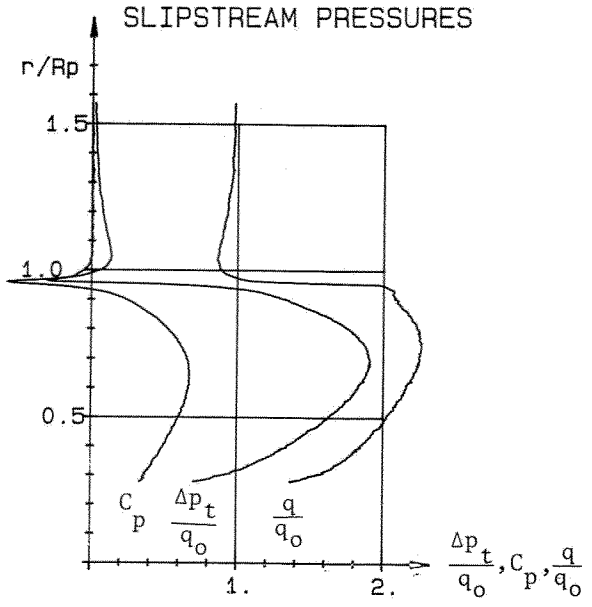

Figure 6a Slipstream pressures: Total, static and dynamic pressures vs radius

CONF1

14.% prop radius downstream distance from prop disk,
φ_s = 90°,
U_∞ = 48.6 m/s, $\alpha = \beta$ = 0°,
$\beta_{.75}$ = 29°, N = 6650 RPM
C_T = 0.232, J = 0.686, C_P = 0.248

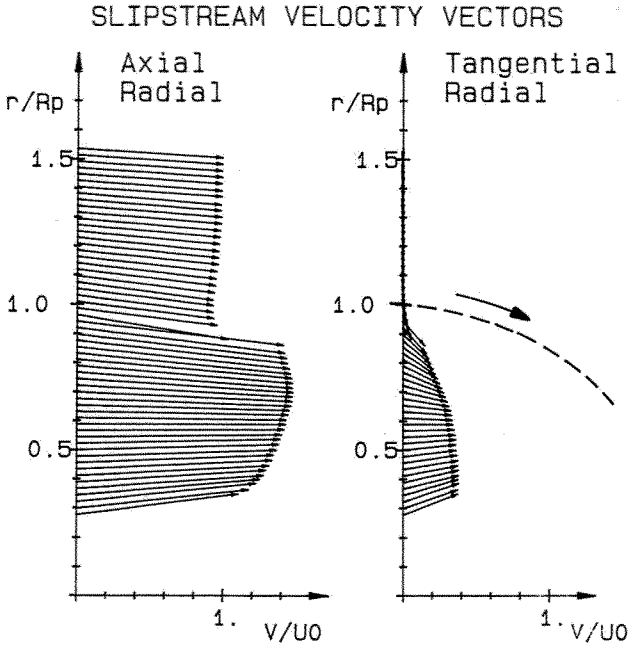

Figure 6b Slipstream velocities vs radius

(Same conditions as in Figure 6a)

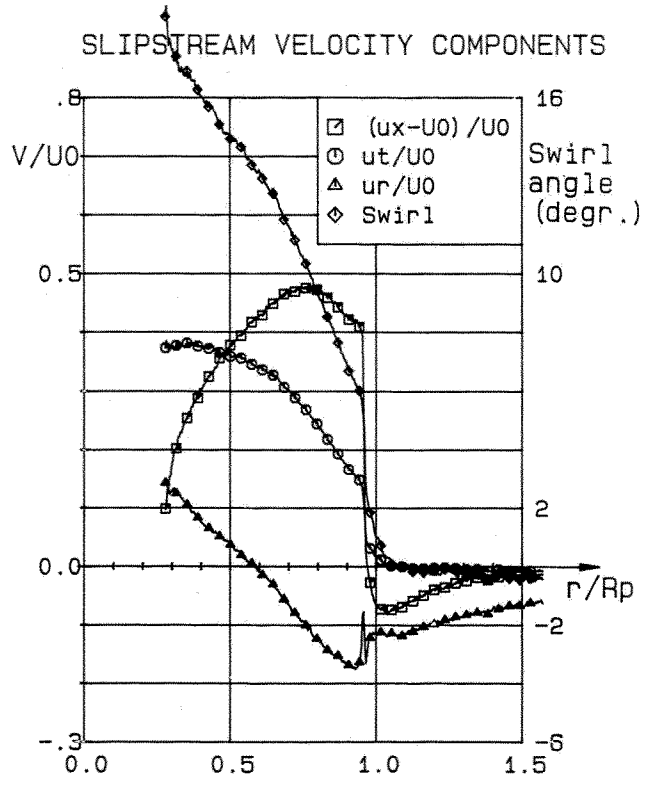

Figure 6c Slipstream velocity components and swirl angle vs radius

(Same conditions as in Figure 6a)

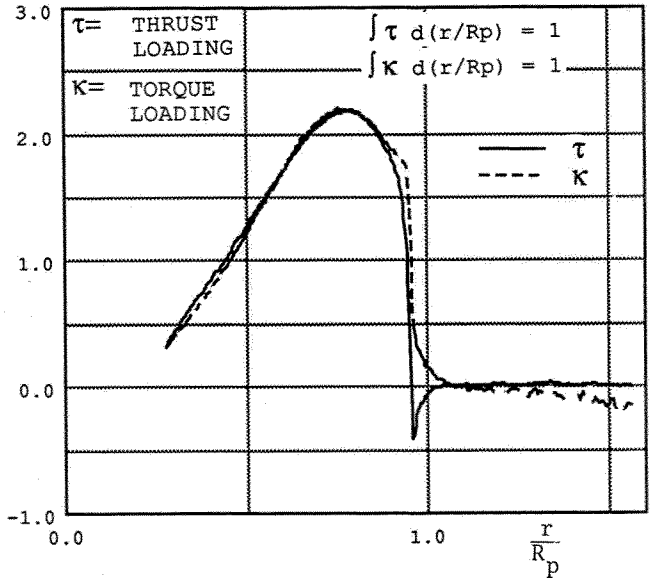

Figure 7 Non-dimensionalized thrust and torque loadings (as obtained by integration of slipstream total pressure and velocities)

(Same conditions as in Figure 6)

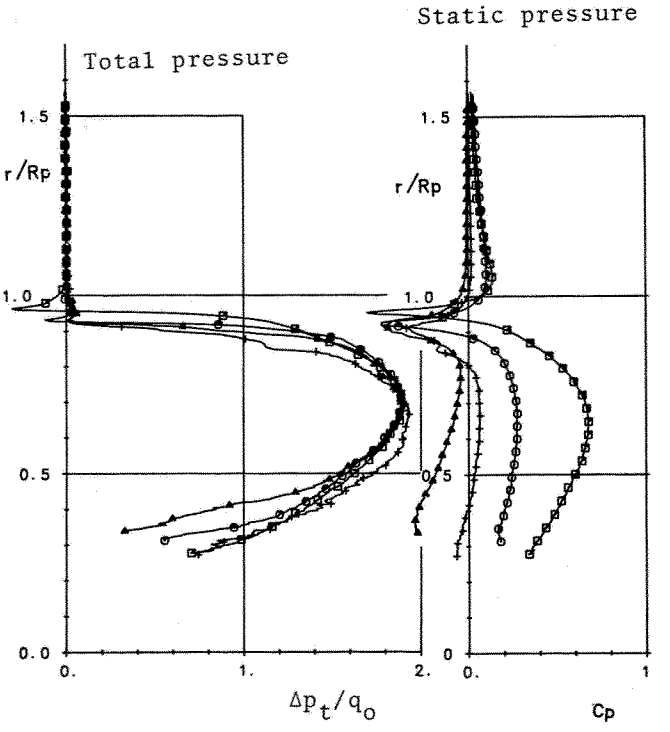

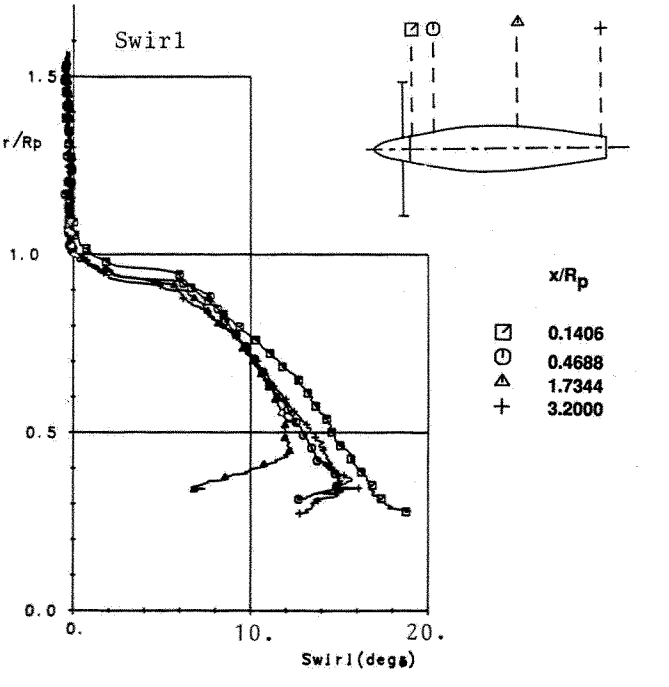

Figure 8 Axial development of slipstream characteristics

CONF1

$\varphi_s = 90^o$
$U_\infty = 48.6$ m/s, $\alpha = \beta = 0^o$,
$\beta_{.75} = 29^o$, N = 6650 RPM
$C_T = 0.236$, J = 0.686, $C_P = 0.253$

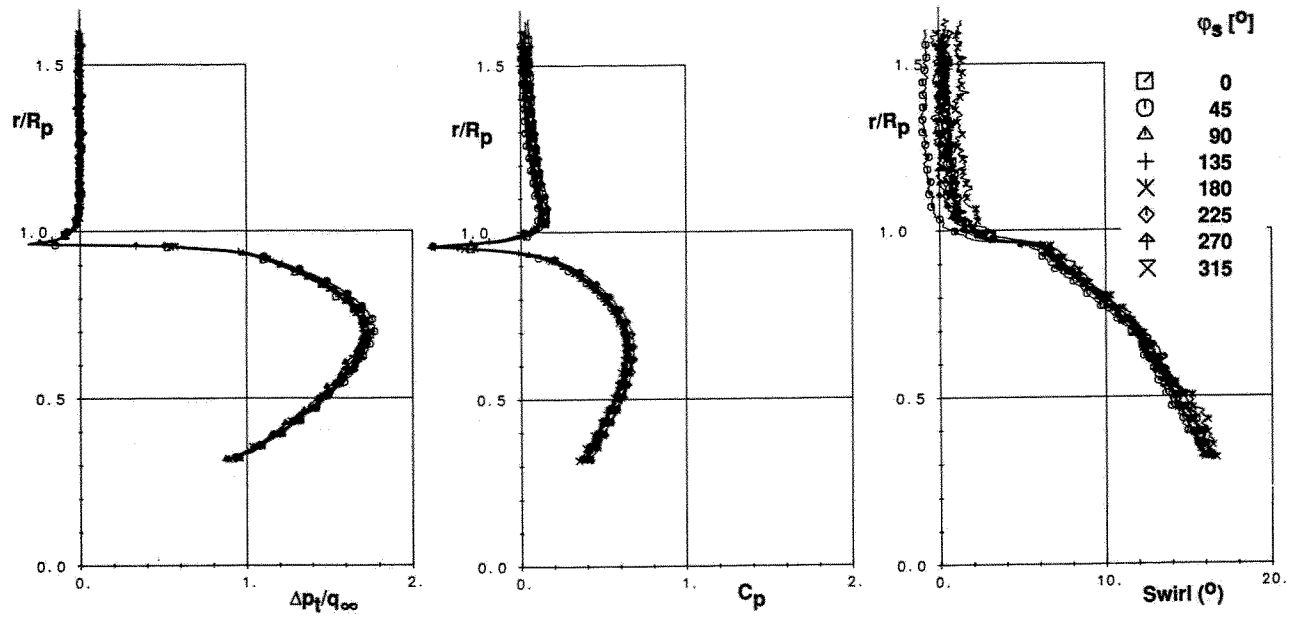

Figure 9 Slipstream survey

CONF2

14 % prop radius downstream distance from prop disk,

U_∞ = 49.6 m/s, $\alpha = \beta = 0^o$,
$\beta_{.75} = 29^o$, N = 6650 RPM
C_T = 0.236, J = 0.698, C_P = 0.242

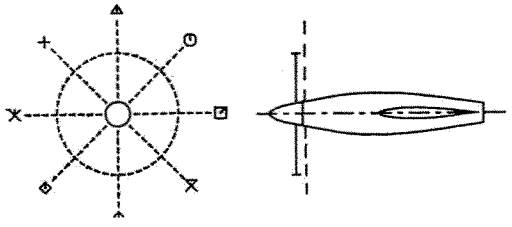

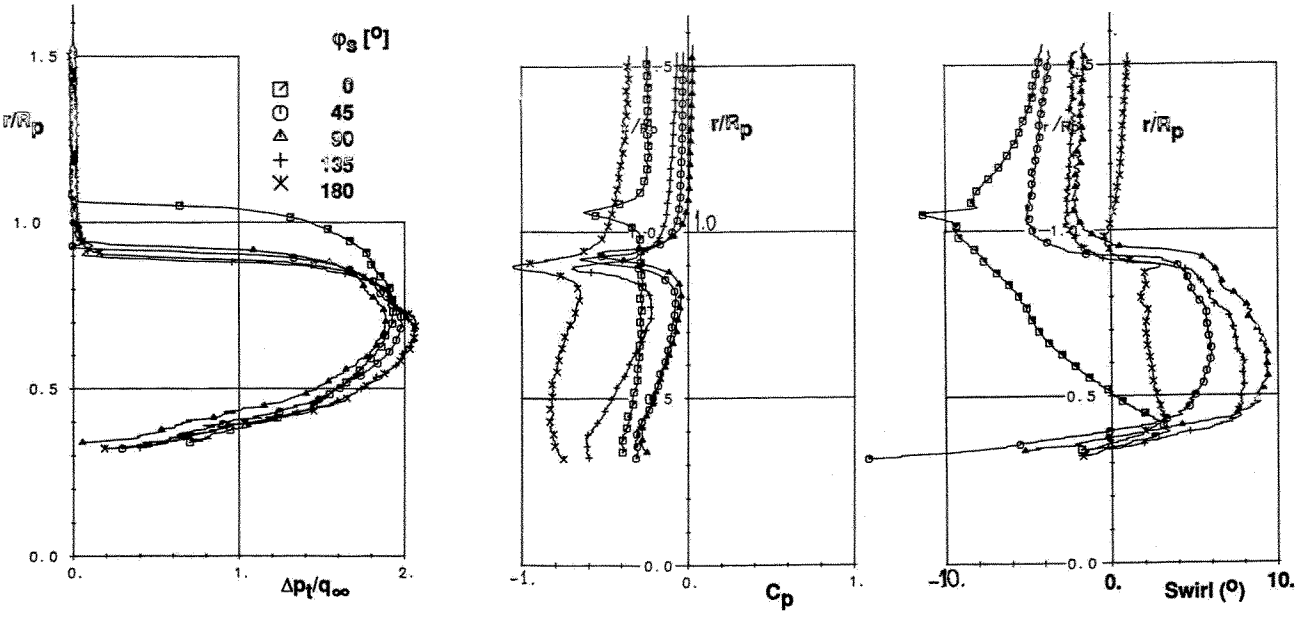

Figure 10a Slipstream survey

CONF2

175 % prop radius downstream distance from prop disk (at wing c/4-plane, above wing)

U_∞ = 48.7 m/s, $\alpha = \beta = 0^o$,
$\beta_{.75} = 29^o$, N = 6650 RPM
C_T = 0.245, J = 0.687, C_P = 0.250

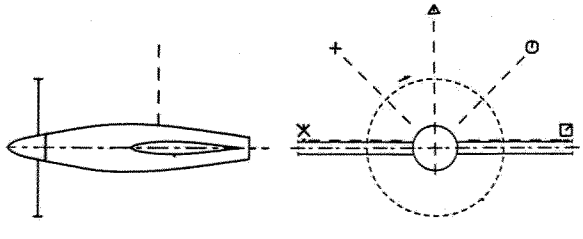

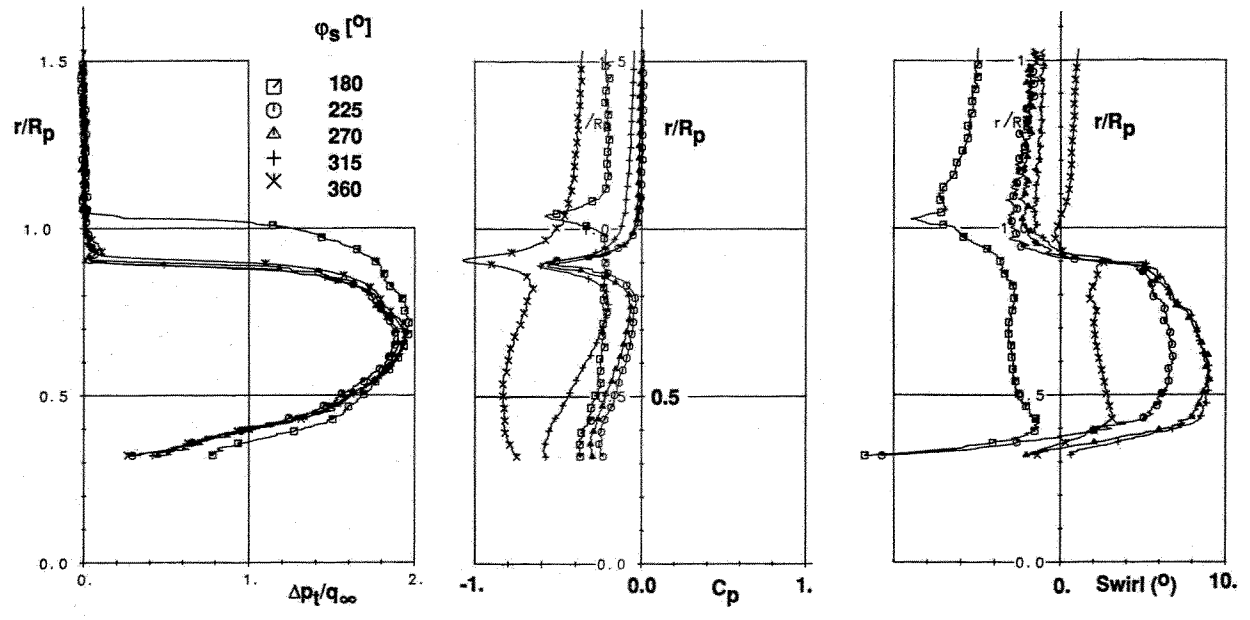

Figure 10b Slipstream survey

CONF2

175 % prop radius downstream distance from prop disk (below wing)

(Same conditions as in Figure 10a)

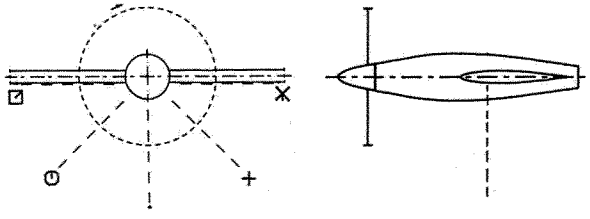

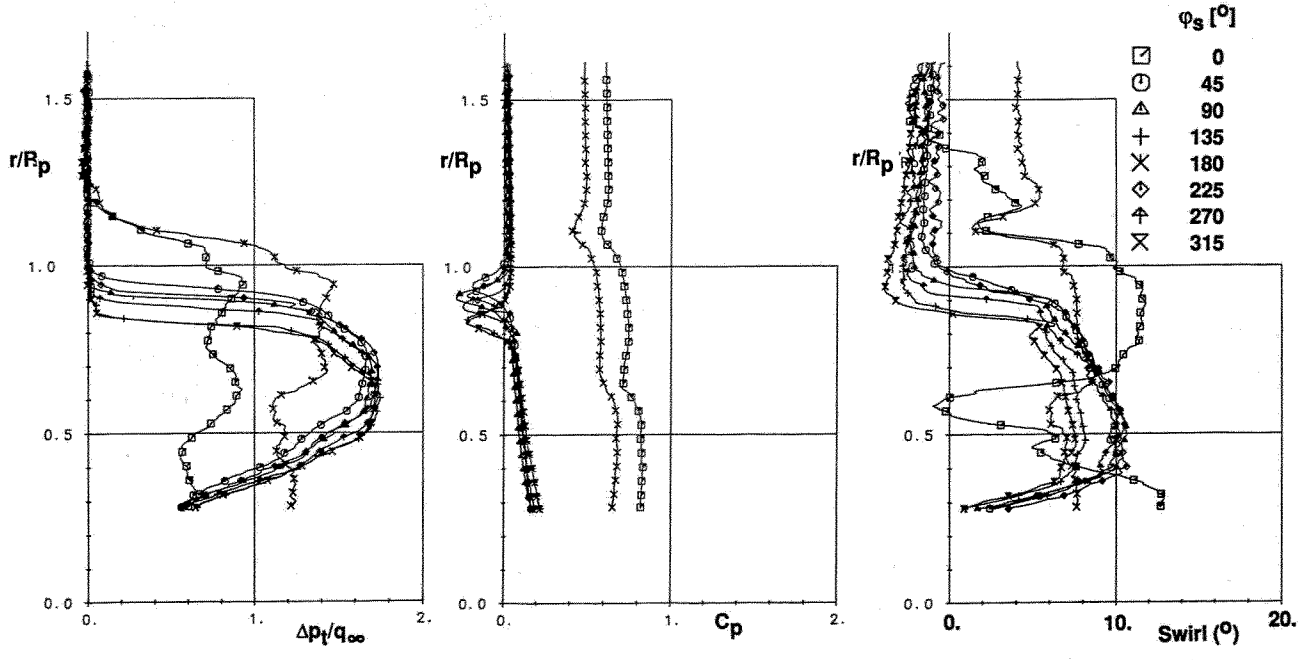

Figure 11 Slipstream survey

CONF2

300 % prop radius downstream distance from prop disk (5 % wing chord downstream wing TE)

U_∞ = 49.7 m/s, $\alpha = \beta = 0°$,

$\beta_{.75}$ = 29°, N = 6650 RPM

C_T = 0.215, J = 0.702, C_P = 0.235

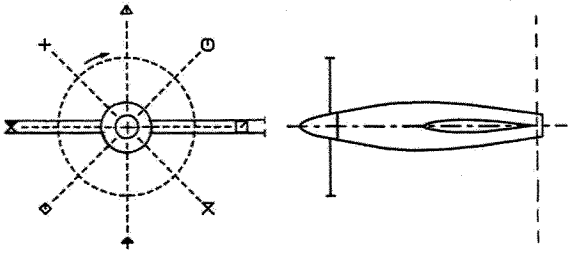

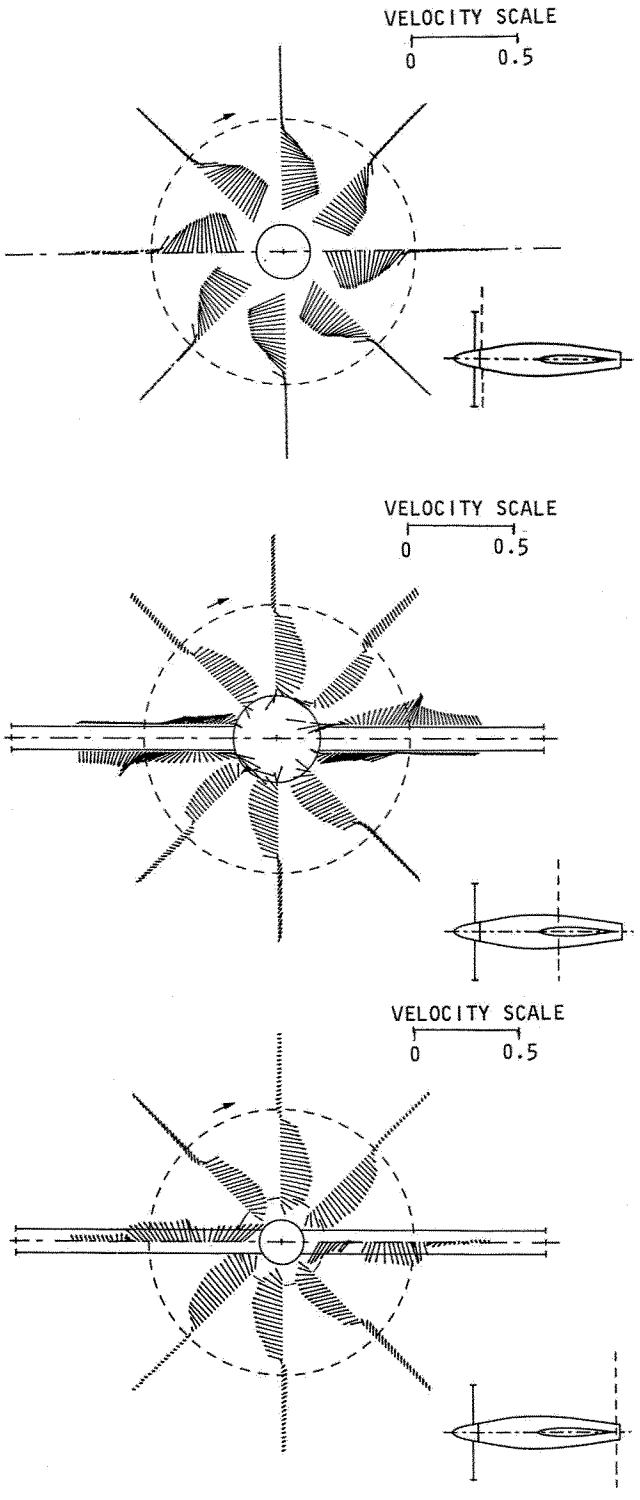

Figure 12 Axial development of slipstream cross-flow

CONF2

U_∞ = 49.3 m/s, $\alpha = \beta = 0^o$,
$\beta_{.75} = 29^o$, N = 6650 RPM
C_T = 0.232, J = 0.696, C_P = 0.242

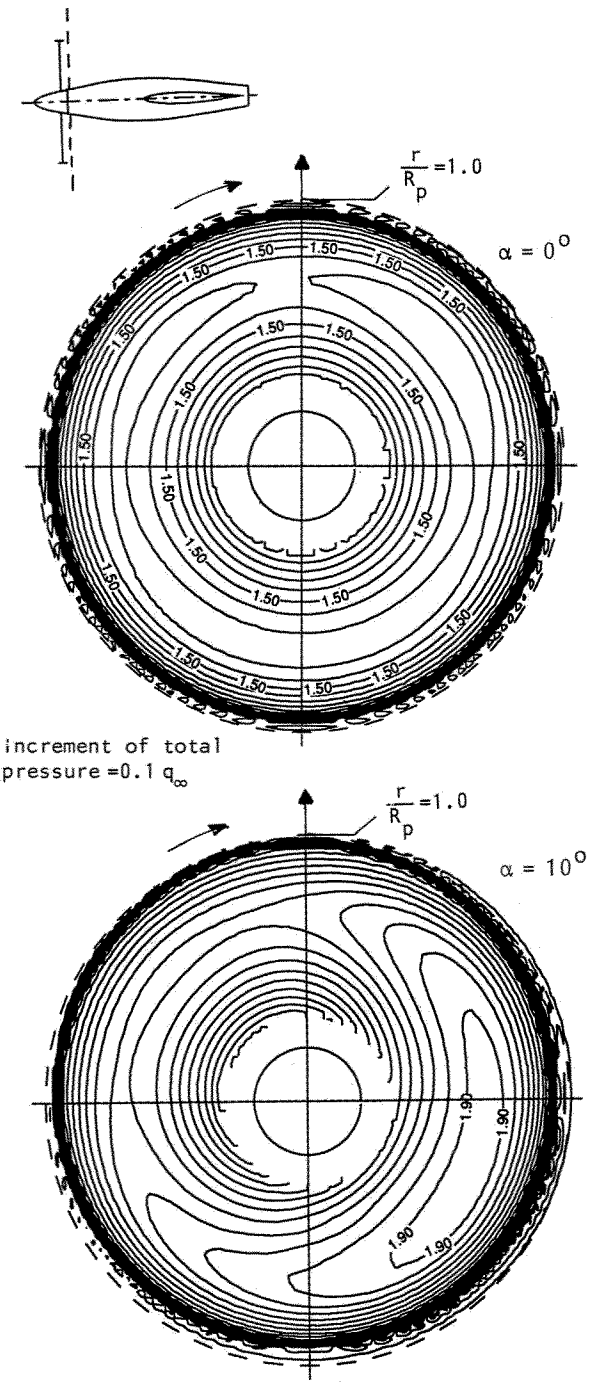

Figure 13 Total pressure distribution (isobar map)

Effect of angle of attack

CONF2

14 % prop radius downstream distance from prop disk

U_∞ = 49.6 m/s, $\alpha = \beta = 0^o$,
$\beta_{.75} = 29^o$, N = 6650 RPM
C_T = 0.235, J = 0.699, C_P = 0.242

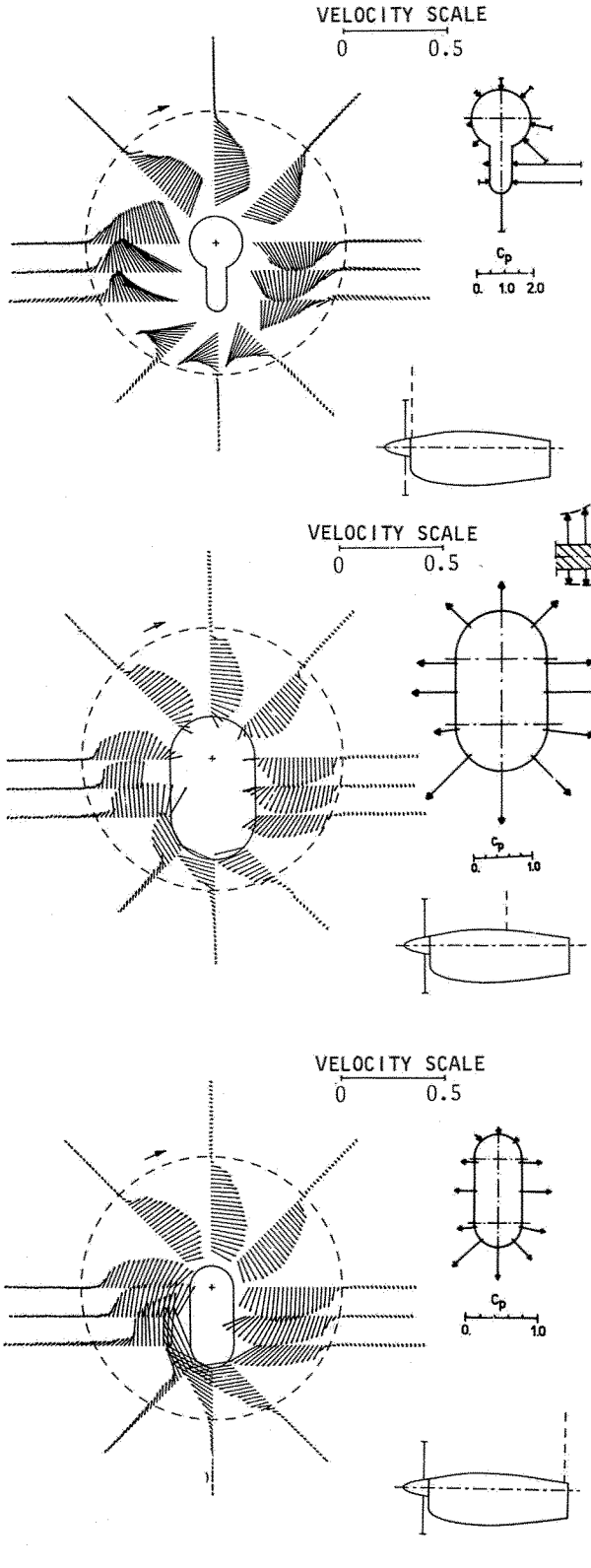

Figure 14 Axial development of slipstream cross-flow

CONF3

U_∞ = 50.0 m/s, $\alpha = \beta = 0^o$,
$\beta_{.75} = 29^o$, N = 6650 RPM
C_T = 0.231, J = 0.705, C_P = 0.225

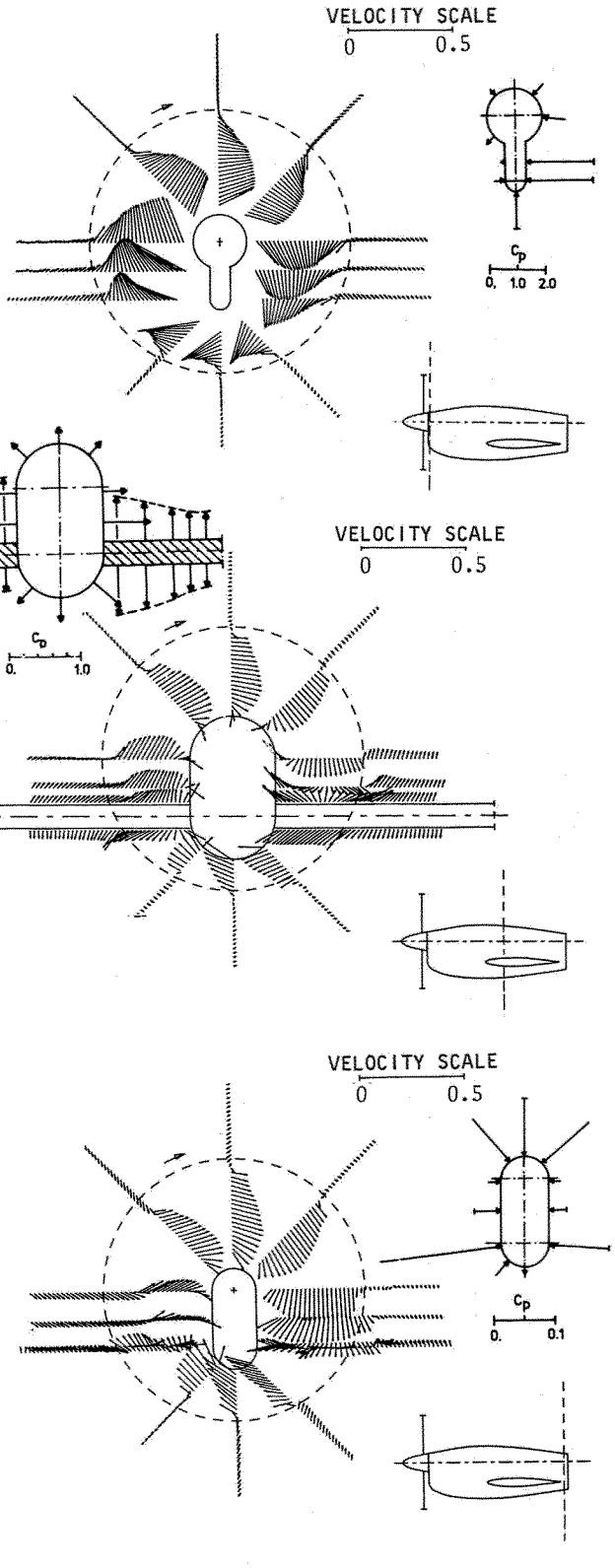

Figure 15 Axial development of slipstream cross-flow

CONF4

U_∞ = 49.8 m/s, $\alpha = \beta = 0^o$,
$\beta_{.75} = 29^o$, N = 6650 RPM
C_T = 0.229, J = 0.705, C_P = 0.232